Study of the Effects of Phytoplankton Morphology and Vertical Profile on Lidar Attenuated Backscatter and Depolarization Ratio

Patrick G. Stegmann[a],*, Bingqiang Sun[b], Jiachen Ding[b], Ping Yang[b], Xaidong Zhang[c]

[a]*Joint Center for Satellite Data Assimilation, NOAA Center for Weather and Climate Prediction, 5830 University Research Ct, 20740 College Park, MD, USA*

[b]*Department of Atmospheric Sciences, Texas A&M University, 3150 TAMU, 77840 College Station, TX, USA*

[c]*Department of Earth System Science and Policy, University of North Dakota, 58202 Grand Forks, ND, USA*

Abstract

Propagation of a lidar beam in a coupled atmosphere-ocean model consisting of multiple atmospheric and upper oceanic layers and a rough ocean surface is studied by using a vectorized Monte Carlo radiative transfer solver optimized specifically for lidar-based remote sensing applications. The effects of assumed phytoplankton morphology variations and its vertical distribution on the lidar attenuated backscatter and depolarization ratio are studied. In this study, a phytoplankton particle is assumed to be a sphere, a sphere with a core, or a randomly distorted hexahedron with or without a core. The single-scattering properties of the nonspherical/inhomogeneous particles are computed using appropriate state-of-the-art light-scattering computational capabilities. Vertical variation of the phytoplankton distribution is derived explicitly using a PAR (photosynthetically active radiation) limited carbon biomass balance equation that is subsequently coupled with the Monte Carlo solver.

Keywords: Monte Carlo; radiative transfer; ocean optics; phytoplankton; lidar; Net Primary Production; remote sensing;

1. Introduction

1.1. Phytoplankton context

Phytoplankton in the oceans accounts for approximately half of the Earth's primary production [1]. Monitoring and assessing the phytoplankton concentration in the sunlit oceans is critical to understanding global carbon cycles [2]. Remotely sensed spectral reflectance observed by, for example, a spaceborne sensor, can provide an estimate of the algal content in the upper layer of the water column [3]. For global carbon cycle or biogeochemical studies involving primary production, such satellite-based observational information about the column-integrated near-surface phytoplankton

_____

* Corresponding author. Tel.: +1-301-683-3522.
E-mail address: patrick.stegmann@noaa.gov

27   concentration is insufficient, and must be extended downward to include the biomass vertical distribution [4].

28   Complementary to passive ocean color measurements, space-based active Light Detection and Ranging (lidar)

29   measurements can be used to effectively retrieve the vertical distribution of water constituents.

30

31   Observations by the CALIOP (Cloud-Aerosol Lidar with Orthogonal Polarization) instrument [5] provides an

32   unprecedented opportunity to accurately measure phytoplankton properties on a global scale. Retrieval of phytoplankton

33   properties using CALIOP data has only recently been demonstrated by Churnside et al. [6] and Behrenfeld et al. (2013) [7].

34   Since then, lidar has drawn further interest as a tool to quantify phytoplankton due to both its global availability and its

35   vertical resolution capability in contrast to passive imaging instruments (e.g. [8]). Schulien et al. [9] show that vertically

36   resolved measurements of phytoplankton biomass and the underwater light field are crucial for accurate measurements of

37   column-integrated phytoplankton net primary production (NPP). To accurately interpret the lidar signal requires a thorough

38   understanding of the measurement process itself, which, in turn, includes the propagation of the lidar beam and the single-

39   scattering properties of phytoplankton. Recent progress in radiative transfer simulation based on the Monte Carlo technique

40   [10] and in light scattering computational capabilities associated with phytoplankton [11] allow us to investigate the

41   sensitivities of lidar measurements to vertical variability in phytoplankton biomass. In particular, the present study is aimed

42   at quantifying the effects of phytoplankton morphology assumptions and phytoplankton population vertical profiles in an

43   oceanic column on lidar attenuated backscatter and depolarization ratio signals.

44

45   This paper is organized as follows. Section 2 describes the Monte Carlo radiative transfer solver used in this study, and also

46   explains the mechanism for treating the ocean-atmosphere interface explicitly, and describes the model setup in terms of the

47   boundary conditions and the decomposition of the computational domain for the radiative transfer solver. Section 3

48   specifies the computational domain in detail, including the solution of the vertically-resolved phytoplankton NPP model in

49   conjunction with the selected phytoplankton morphologies and relevant light scattering computations. Section 4 presents a

50   sensitivity study of the variations of the model parameters. Section 5 concludes this study by summarizing its findings.

51   **2. Polarized Monte Carlo radiative transfer code for lidar applications**

52   *2.1. Theoretical background*

53   To compute the attenuated backscatter and depolarization ratio measured by a space based lidar instrument the stationary

54   monochromatic vector radiative transfer equation (RTE) is solved (see [12,13] for details and fundamental assumptions

55   involved in the derivation of the RTE from first principles):

56
$$\left(\omega\cdot\nabla\right)\vec{I}(\vec{x},\omega) = -b_{ext}(\vec{x})\cdot\vec{I}(\vec{x},\omega) + b_{scatt}(\vec{x})\int_{S^2}P\left(\omega\cdot\omega'\right)\cdot\vec{I}(\vec{x},\omega')d\omega', \qquad (1)$$

57   where ω is the 3D unit direction vector, $\vec{x}$ the position vector in 3D Euclidean space, b_{ext} the extinction coefficient,

58    $b_{scatt}(\vec{x})$ the scattering coefficient, S^2 the unit sphere, $P\left(\omega\cdot\omega'\right)$ the phase matrix, ω / ω' the unit incident/scattered

59   directional vector, and $\vec{I}(\vec{x},\omega)$ the 4x1 Stokes vector. It should be noted that if the transient dynamics of the lidar laser

60   pulse are of interest, the fully time-dependent RTE should be solved using such methods as e.g. applied in [14]. Furthermore

61   Eq. (1) requires the assumption that the host medium is nonabsorbing, which is justified for the visible band but not in the

62   infrared. In this case, both the radiative transfer calculations and the single-scattering computations need to be modified

63   according to [15,16]. Eq. (1) does not contain sources and the boundary conditions are given by an absorbing lower

64   boundary in the ocean and the lidar laser beam at the top of the atmosphere (TOA):

$$\vec{I}_{TOA}(\vec{x},\omega) = \begin{pmatrix} I_0 \\ Q_0 \\ 0 \\ 0 \end{pmatrix} \cdot \delta(\vec{x}_0) \cdot \delta(\omega_\sphericalangle), \tag{2}$$

66   where $\delta(\omega_\sphericalangle)$ is the Dirac delta function for the divergence angle of the linearly polarized laser beam of the lidar

67   instrument. Integrating Eq. (1) along a constant direction ω leads to the following integral equation for the Stokes vector:

$$\vec{I}(\vec{x},\omega) = \int_0^\infty \exp\left(-\int_0^u b_{ext}(\vec{x}_v)\,dv \right) \cdot b_{scatt}(\vec{x}_u) \int_{S^2} P(\omega \cdot \omega') \cdot \vec{I}(\vec{x}_u, \omega')\,d\omega'\,du, \tag{3}$$

69   where $\vec{x}_u = \vec{x} - u \cdot \omega$. Eq. (3) is a Fredholm integral equation of the second kind with the exponential factor being the so-

70   called transport kernel and the phase matrix as the collision kernel. The high-dimensional integral in Eq. (3) can be

71   computed using Monte Carlo integration [17] and thus an expectation value for $\vec{I}(\vec{x}, \omega')$ can be estimated. Eq. (3)

72   motivates the use of the Monte Carlo method on purely mathematical grounds without recourse to the troublesome concept

73   of the photon corpuscle.

74   *2.2. Computational domain*

75   A model setup is schematically illustrated in Fig. 1. The coupled atmosphere-ocean system is modeled as a layered column

76   with the sea surface as an infinitely thin specular interface at the vertical Cartesian coordinate z_{ocean}. Scenarios involving

77   atmospheric scattering layers, such as clouds or aerosol layers are only addressed in this paper in order to validate the Monte

78   Carlo code, but not for the sensitivity studies involving phytoplankton. Ocean layers may contain multiple plankton layers

79   with the only requirement that layers cannot overlap. Each layer is completely defined by geometrical top and bottom

80   heights and a set of appropriate single-scattering properties for the desired type of scattering particles. Molecular scattering

81   is explicitly included in both the atmosphere and ocean. The space-based lidar is placed at TOA and has a given laser beam

82   divergence angle and sensor aperture angle. The laser beam divergence in particular is explicitly considered in the sampling

83   of the boundary condition Eq. (2), and the sensor aperture is explicitly taken into consideration in the computation of the

84   expectation value of Eq. (3) via the variance reduction technique discussed in the next subsection. The lidar beam

85   propagates downward through the scattering layers. The lidar receiver receives the scattered light, depending on the off-

86   nadir angle of the beam and the specular reflection from the ocean surface. It is important to emphasize, that the full 3D

87   RTE is solved in each calculation. However, due to the layered nature of the model setup only a pseudo-1D solution is

88   feasible under the condition that the and terrestrial curvature effects are neglected because of the layered nature of the model
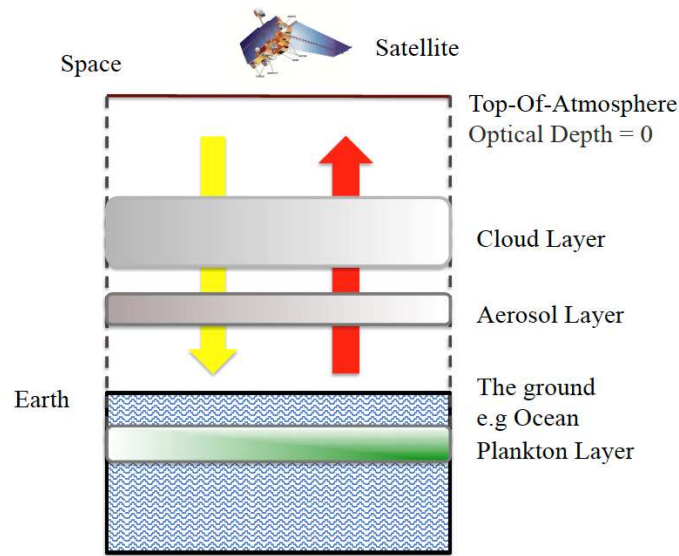
89   setup.

90

91   Figure 1: Sketch of the computational domain. Cloud layers are shown in grey, aerosol layers shown in brown, phytoplankton layers shown in green and
92   water shown in blue.

93   *2.3. Monte Carlo solution and variance reduction technique*

94   The specific Monte Carlo approach used in this study is a method optimized for lidar applications was originally published

95   in [18] for the scalar case and later extended to the fully polarized case [10]. The Monte Carlo algorithm is fully described

96   in detail in [10]. However, this study extends the original algorithm to a coupled atmosphere-ocean system, because the

97   original algorithm is only suitable only for atmospheric applications involving scattering by atmospheric particles, such as

98   clouds and aerosols. The modifications are:

99   • Accounting for specular reflection and refraction of radiation at the ocean interface in the Monte Carlo integration

100   process.

101   • Accounting for specular refraction at the ocean interface in the variance reduction technique.

102   • Explicit treatment of (molecular) Rayleigh scattering in both atmosphere and ocean.

103

104   While counterintuitive at first glance, the representations of the ocean surface in the first and second modification are

105   different. Globally the Monte Carlo algorithm used in this study can be divided into conventional iterative forward Monte

106   Carlo ray tracing, where the free path and scattering direction are sampled on an alternating basis, and the additional

107   variance reduction step. The variance reduction technique used in this study, as well as in the previous studies [10,18], is

108   referred to as the *analytic fraction trace* [sic], which, in essence is the same as the *local estimate method* reported in [19,20].

109   Basically, the expected value of the Stokes vector measured by the lidar instrument is computed from the contributions of

110   all Monte Carlo paths that are scattered *directly* into the sensor at *each* collision event (scattering and intersecting the ocean

111   interface for the present problem). After the collision event, the expected value of the sensor signal is increased by the

112   contribution of the directly scattered Stokes vector, and the Monte Carlo path is diminished by the corresponding amount.

113

114   In the conventional Monte Carlo ray tracing technique, two possible methods exist to treat the ocean interface and the

115   necessary specular reflection and refraction of the light rays. The first method is conventional recursive ray tracing, where

116   each ray is split up into a reflected and refracted ray that is then recursively traced onward (see e.g. [21] for an early

117   reference). The second approach is to extend the Monte Carlo philosophy to the refraction process as well, and let each

118   Monte Carlo path refract **or** reflect based on statistical sampling, such that the Fresnel equations are fulfilled in the limit of a

119   large number of light rays incident on the interface. In this study, the second approach was selected due to its considerably

120   simpler implementation. The necessary criteria for the statistical approach are given by Mobley in [22]. For polarized light,

121   the polarized reflectances are defined as follows:

$$\rho_{\perp} = \left(\frac{n_i \cos(\theta_i) - n_t \cos(\theta_t)}{n_i \cos(\theta_i) + n_t \cos(\theta_t)} \right)^2, \qquad (4a)$$

$$\rho_{\parallel} = \left(\frac{n_t \cos(\theta_i) - n_i \cos(\theta_t)}{n_t \cos(\theta_i) + n_i \cos(\theta_t)} \right)^2, \qquad (4b)$$

$$\rho(\theta_i, \theta_t) = \frac{\rho_{\perp} + \rho_{\parallel}}{2}, \qquad (4c)$$

125   where subscripts i and t stand for incident and transmitted properties and the variables θ and n are angles and refractive

126   indices respectively. After drawing a uniformly distributed random number q on the interval $\left[0,1\right]$, the condition for a

127   light ray associated with q to be reflected can be written as $q \le \rho(\theta_i, \theta_t)$, based on Eqs. (4). In the complementary case the

128   light ray is counted as transmitted. The angle of refraction θ_t is determined from Snell's law and the normal vector of the

129   ocean surface. For practical calculations the form given in [18,22] is used. The refractive index of sea water was chosen as

130    $n = 1.333$. Under perfectly calm conditions the ocean surface normal points directly upwards in the positive Cartesian z-

131   direction. To simulate a realistic rough ocean interface, the widely used Cox-Munk model [23] is applied in this study. The

132   sampling of a random normal vector resulting from a rough windblown ocean surface with Cox-Munk statistics is

133   performed in the same way as was done in [24] for the case of roughened ice crystals. The contribution of the wave height

134   to the ocean interface height z_{ocean} is assumed to be small and has been neglected in the current model. Other possible

135   alternatives that would provide increased realism rely on generating an ensemble of ocean surface realizations based on the

136   Fourier transform technique discussed by Mobley in [25] or by directly solving the shallow water equations for a suitable

137   forcing ([26] provides uncertainties as well). However, for the purposes of this study, the Cox- Munk model is sufficient, as

138   the influence of the ocean surface roughness is not the primary focus of this investigation and as shown in Table 1 and Fig.

139   10 of [25], the agreement between the FFT and Cox-Munk model is close.

140

141   Considering the ocean interface in the analytic fraction trace variance reduction mechanism is a subtler issue compared to

142   its treatment in Monte Carlo ray tracing. First of all, the variance reduction technique remains unaffected as long as the

143   collision takes place *above* the ocean surface. If this is not the case, the semi-analytic estimate of the lidar signal given in

144   [10,18] needs to be multiplied by the transmittance matrix of the ocean surface, as the Fresnel refraction diminishes the

145   Stokes vector contribution further:

146
$$\vec{E} = \vec{I}\left(\vec{x}, \omega\right) \cdot \varpi \cdot \Delta\Omega_{dish} \cdot \exp\left(\frac{b_{ext} \cdot \Delta d}{cos(\theta_{scatt})}\right) \cdot \mathbf{T_S}\left(\theta_i, \theta_t\right), \tag{5}$$

147   where $\vec{E}$ is the contribution to the expectation value of the measurement from an individual collision event, ϖ is the

148   single scattering albedo of the scattering medium, $\Delta\Omega_{dish}$ is the aperture angle of the lidar sensor, Δd is the geometrical

149   distance between the scattering event and the detector, θ_{scatt} is the angle between the direction of the light ray before the

150   collision event and the direction towards the lidar aperture cone, and $\mathbf{T_S}\left(\theta_i, \theta_t\right) \in {}^{4\times4}$ is the Fresnel transmissivity matrix

151   of the ocean surface S with elements T_{ij} shown in Figs. 3 and 4. As pointed out by Kattawar [27] and Mobley [25], the

152   proper transmissivity matrix to be used in Monte Carlo calculations is the transmissivity matrix for irradiance. This

153   contrasts with the transmissivity matrix for radiance, where the beam of light is considered to have a finite cross-section,

154   which changes upon refraction, as illustrated in Fig. 2.
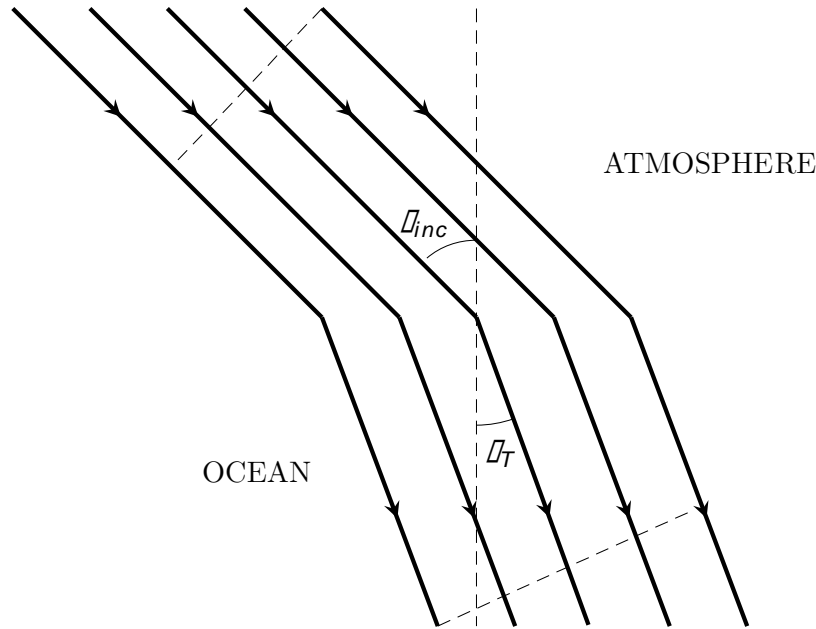
155

156

157   Figure 2: Upon refraction from the incident angle θ_{inc} to the transmitted angle θ_T at the atmosphere-ocean interface, a beam of light rays with a finite
158   cross-section changes its solid angle.

159

160   The difference in the matrix elements is illustrated in Figs. 3 and 4 together with the difference in the reflectivity matrix

161   elements. The proper transmissivity matrix used for Eq. (5) is given in [27,28]. The transmissivity matrix elements as a

162   function of incidence angle used in this study are shown in Fig. 3 in solid lines.
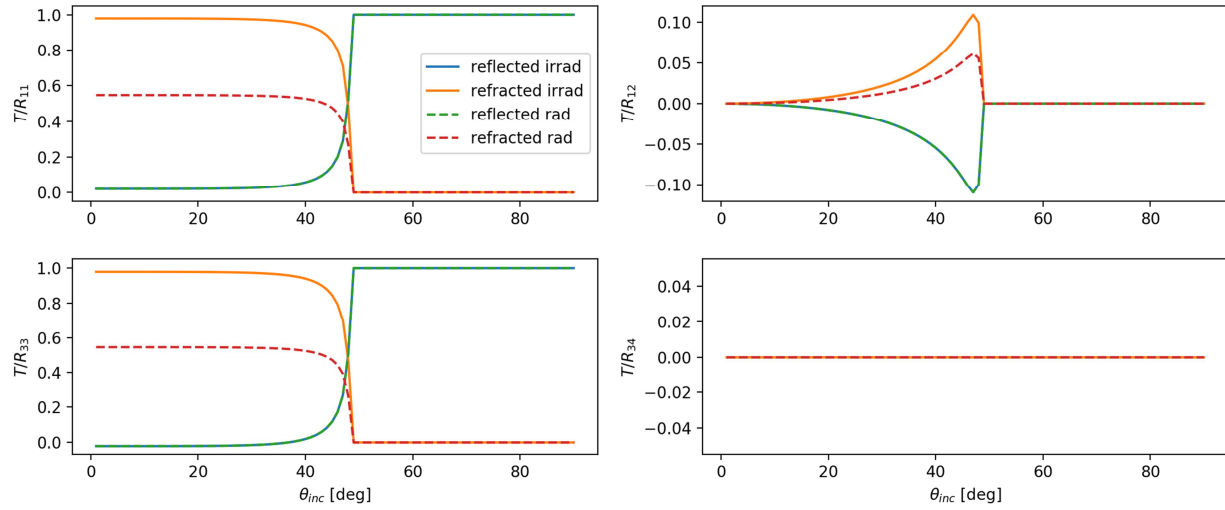
163

Figure 3: Comparison of reflectivity and transmissivity matrix elements of an ocean-atmosphere interface for radiance and irradiance. The values of the refractivity curves in orange color are used in Eq. (5). Light ray is leaving the ocean and entering the atmosphere.
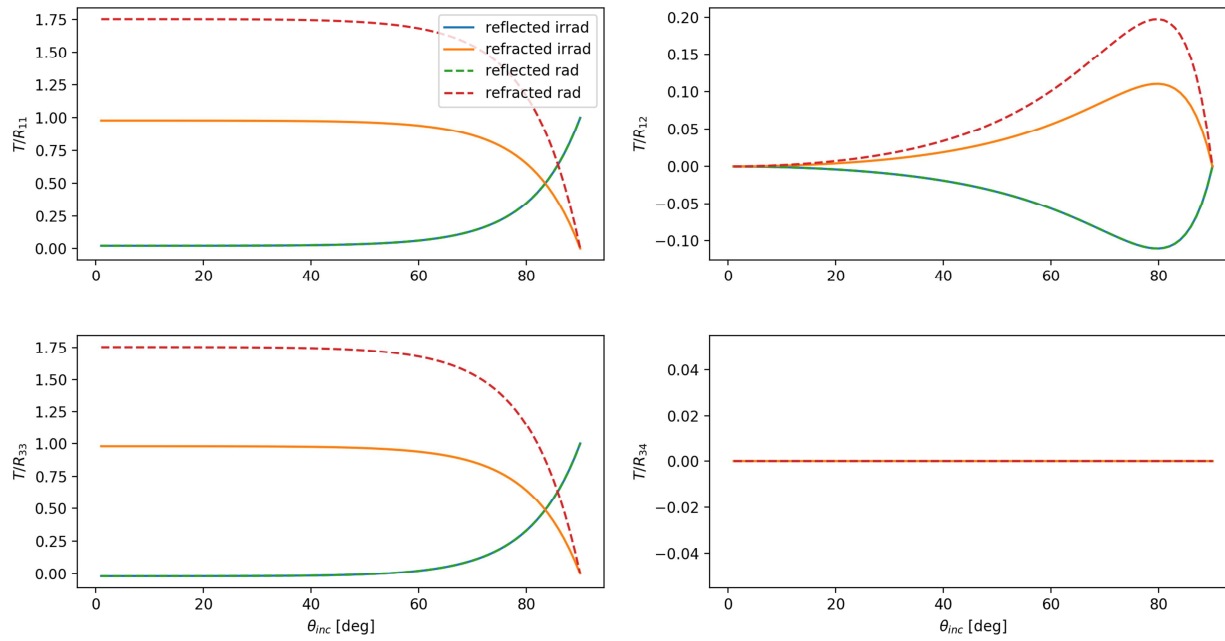
166

Figure 4: Comparison of reflectivity and transmissivity matrix elements of an ocean-atmosphere interface for radiance and irradiance. Light ray is leaving the atmosphere and entering the ocean.

169   **3. Description of phytoplankton and coupled atmosphere-ocean model**

170   *3.1. Atmospheric model*

171   An atmospheric description has also been included in each Monte Carlo radiative transfer calculation. The Rayleigh
172   scattering optical thickness is relatively large at lidar wavelengths 355 nm and 532 nm, and the algorithms necessary for
173   considering an inhomogeneous plankton profile allow the explicit treatment of Rayleigh scattering from the overlying
174   atmospheric column with little extra effort. The Rayleigh scattering extinction profile is calculated based on the
175   Atmospheric Attenuation Model, 1964 [29]. Figure 5 shows the obtained mass density of air, which is linearly proportional
176   to the Rayleigh extinction coefficient, in conjunction with an example discretization of the coefficient profile for the layers
177   varying with height. The necessary data, including density profile, molecular mass relative to carbon 12, and Rayleigh
178   attenuation coefficient of *air* at 532 nm are given in [29,30].
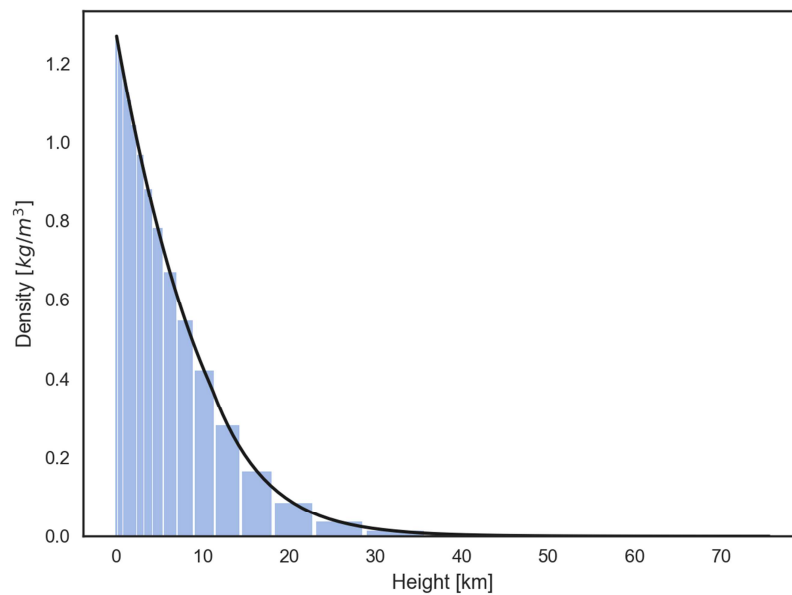

179

180   Figure 5: Density layers (blue bars) with logarithmic layer spacing (the plot scale is linear) based on barometric density data (black curve).

181   The Müller matrix for Rayleigh scattering used in the Monte Carlo calculations has been taken from [31] and its elements
182   are depicted in Fig. 6. In practice, only the lowest and thus densest three layers of the atmosphere are used.
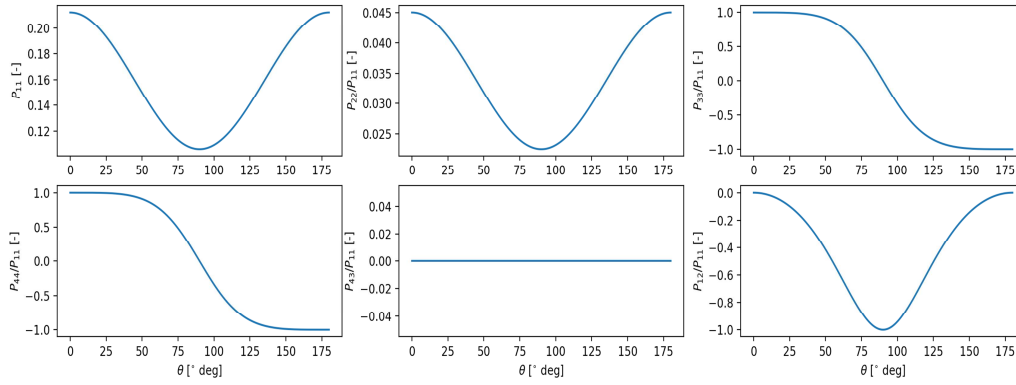
Figure 6: Müller matrix elements for (molecular) Rayleigh scattering based on [28].

3.2. Vertically resolved phytoplankton distribution model

In order to synthesize vertically inhomogeneous profiles of the phytoplankton concentration, several possible approaches have been developed and it is *a priori* not clear, which one is the most appropriate for the purpose at hand. One possible approach is based on a reaction-diffusion-advection equation [32-35] that describes the phytoplankton population balance as a function of space and time. Based on the review [36] by Westberry and Behrenfeld, the empirical depth-resolved carbon-based model by Westberry et al. [37] has been chosen, however, as it is more suited to remote sensing applications and the approach of using a reaction-diffusion-advection equation is unrecognized in the phytoplankton remote sensing community itself. The simple model proposed in [37] predicts the vertically resolved NPP profile based on the carbon biomass $C(z)$ of the phytoplankton as a function of the ocean depth z:

$$
\begin{aligned}
C(z) &= C_{z=0} & if \quad R \le \mu(z) \\
C(z) &= C_{z=0} \cdot \left(\frac{\mu(z)}{R} \right) & if \quad R > \mu(z)
\end{aligned}
\quad ,
\tag{6}
$$

where $C_{z=0} = 10.5 \, mg \, C \cdot m^{-3}$ is the phytoplankton carbon biomass density at the ocean surface $z = 0$, $R = 0.1 d^{-1}$ is the background loss rate parameter, and $\mu(z)$ is the phytoplankton growth rate in units of $[d^{-1}]$. If not otherwise mentioned, parameter values and notation have been taken directly from [37]. Inside the mixed layer the carbon biomass is assumed to stay constant as well. Below the mixed layer depth (MLD), the phytoplankton NPP is governed by the light-limited environment and biological photoacclimation processes, as described in [37]. Further details on the computation of $C(z)$ and $\mu(z)$ are given in [37], with the exception of the PAR distribution, whose computation in the context of this work is explained in more detail in the following. For the NPP model of [37] a simple Beer-Lambert attenuation process of the PAR in units of $[mol \cdot m^{-2} d^{-1}]$ by the phytoplankton is proposed, which is a common assumption for such a model [38]:

204
$$PAR(z) = \int_{400}^{700} E_d(0,\lambda) \cdot e^{-\int_0^z K_d(\lambda)dz} \, d\lambda, \qquad\qquad (7)$$

205   where $E_d(0,\lambda)$ is the spectral irradiance at the ocean surface, λ the wavelength in $[nm]$ and $K_d(\lambda)$ is the spectral

206   diffuse attenuation in $[m^{-1}]$. Outside the context of phytoplankton optics it is an interesting albeit so far inconsequential

207   coincidence that Eq. (7) is formally equivalent to a partition function for a classical continuous system in statistical

208   mechanics, or through Wick rotation [39] to a path integral [40], where $E_d(0,\lambda)$ is the initial wave function and

209    $\int_0^z K_d(\lambda) \, dz$ is the Euclidean action.

210   It is beyond the scope of this work to perform radiative transfer calculations to sample $E_d(0,\lambda)$ under different

211   atmospheric conditions and thus Planck's law at 5800 K [41] over the desired spectral range shown in Fig. 7 has been

212   chosen as the PAR source, assuming the earth's atmosphere to be sufficiently transparent over the 400-700 nm wavelength

213   range. In order to match the PAR units used in [37], the Planck function needs to be divided by the energy of individual

214   photons at the given wavelength and should be multiplied by the ocean surface transmissivity at normal incidence to

215   approximately account for the specular reflection of the water surface.

216

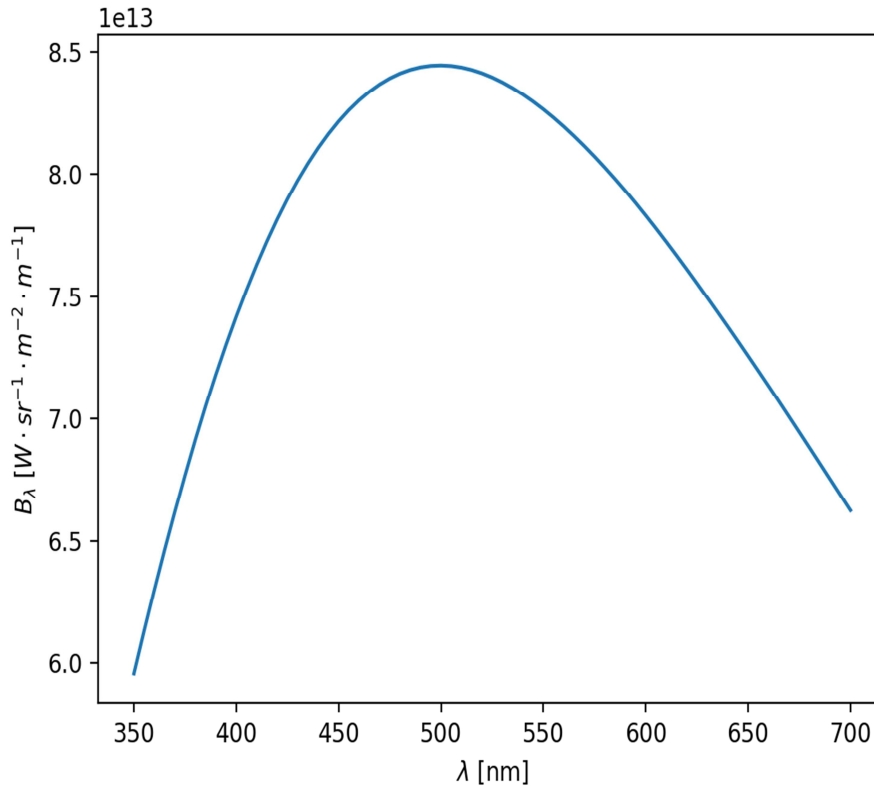217   Figure 7: Planck's law at 5800K as the PAR spectral irradiance source $E_d(0,\lambda)$ at the ocean surface.

218   As in [37], the model for the spectral attenuation $K_d(\lambda)$ has been taken from the work of Morel and Maritorena [42]. Here

219   the spectral attenuation is represented as the sum of the attenuation due to water and the attenuation due to biological

220   components:

221    $$K_d(\lambda) = K_w(\lambda) + K_{bio}(\lambda). \qquad (8)$$

222   Retrieved data for $K_w(\lambda)$ are given directly in [42] and plotted in Fig. 8. Attenuation resulting from dissolved organic

223   matter is calculated as a function of the chlorophyll concentration Chl:

224    $$K_{bio}(\lambda) = \chi(\lambda) \cdot Chl^{e(\lambda)}, \qquad (9)$$

225   where the values for the scaling factor $\chi(\lambda)$ and the exponent $e(\lambda)$ have again been retrieved from [42] and plotted in

226   Fig. 8. In order to read the parameter values from [42] for further processing quickly and without errors, the optical

227   character recognition method developed in Ref. [43] was used again to great effect. As described in [37], photoacclimation

228   leads to a complex relationship between the chlorophyll concentration $Chl(z)$ and the phytoplankton carbon biomass

229    $C(z)$, which in turn depends on $PAR(z)$. This makes it necessary to iteratively solve for the desired vertically resolved

230    $C(z)$ profile. A sample profile of $PAR(z)$ based on Eq. (7) for a constant $Chl(z) = 0.1\, mg\, Chl \cdot m^{-3}$ distribution (i.e.

231   without photoacclimation) is shown in Fig. 9.
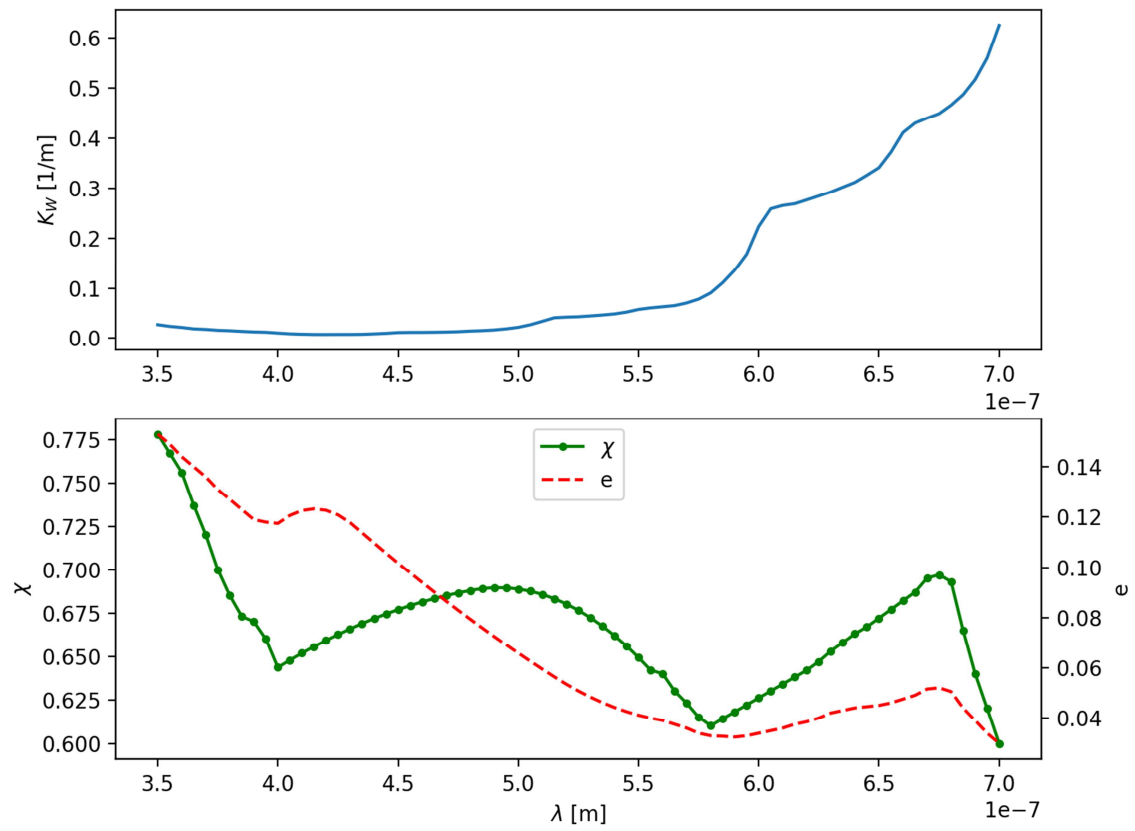
232

233   Figure 8: Retrieved parameter data for Eqs. (8) and (9) from Ref. [42].
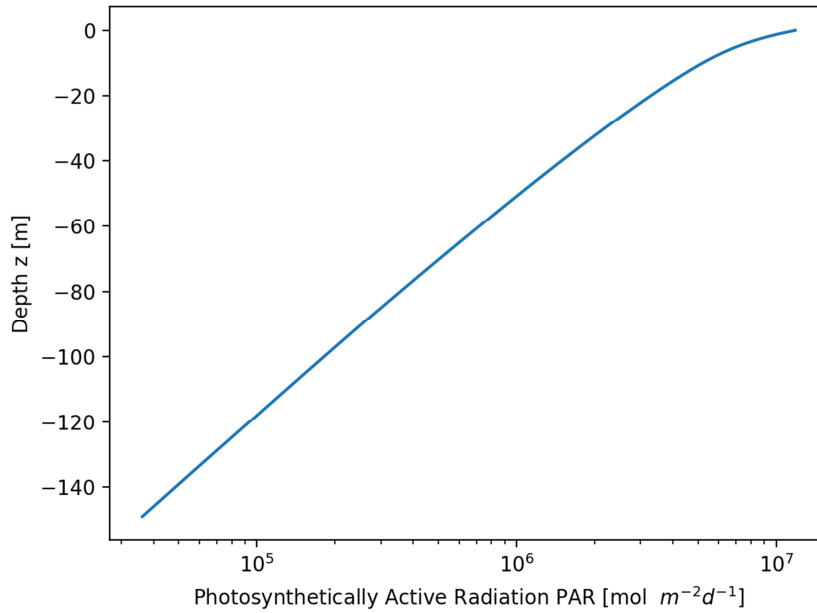
234

Figure 9: A sample profile of $PAR(z)$ based on Eq. (7) for a constant $Chl(z)$ distribution.

235

236

237 For a mixed layer depth of $z_{MLD} = 83\, m$ (indicative of tropical and subtropical waters) Eq. (6) has been solved along the

238 lines of the procedure outlined in [37,42] and the result is shown in Fig. 10. As can be seen, the phytoplankton carbon

239 biomass remains constant in the mixing layer and slightly below z_{MLD}. At greater ocean depths the carbon biomass

240 distribution declines rapidly due to the limited phytoplankton growth rate as a consequence of the PAR attenuation. The

241 Fortran source code used to compute the profile in Fig. 10 is available as supplemental material to this publication. Global

242 mixed layer depth data for further analysis is available e.g. from the Ocean Productivity website of Oregon State University

243 (http://www.science.oregonstate.edu/ocean.productivity/mld.html). A global analysis however is beyond the scope of this

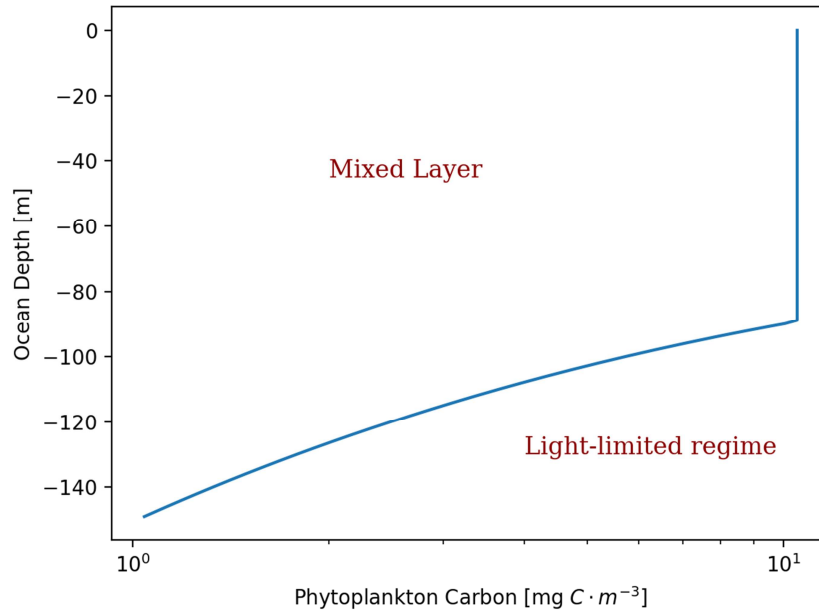244 study. The influence of a nutrient limited environment has likewise been neglected.

245

Figure 10: A sample profile of $C(z)$ for an MLD of 83 m. Note the rapid and smooth decline of phytoplankton carbon density below the MLD.

247 For the Monte Carlo calculations themselves, the profile in Fig. 10 has been down-sampled and discretized in terms of

248 layers, as illustrated in Fig. 4 for the case of the atmosphere.

249 *3.3. Phytoplankton single-scattering properties*

250 From the perspective of electromagnetic scattering, phytoplankton are generally characterized as optically thin particles

251 with small indices of refraction relative to the surrounding medium (water), while the size parameter of individual particles

252 can become very large (in relation to other light scattering particles) and many phytoplankton morphologies exist, some of

253 which are not necessarily convex [44]. A number of techniques have been developed to cope with the non-spherical

254 morphologies and large size parameters, and to benefit from the low refractive index contrast. Specifically mentioned are

255 the anomalous diffraction for spherical scatterers, as discussed by van de Hulst in [45], the many-body iterative T-matrix

256 (MBIT) method by Sun et al. [46] for chain-like particles, and the implementation of Schiff's approximation by Charon et

257 al. [47] for large particles. Due to the low refractive index gradient, the Discrete Dipole Approximation (DDA) method

258 calculations can also be carried out at relatively large size parameters [48]. For the purposes of this study the sensitivity of

259 the lidar attenuated backscatter and depolarization ratio to the following phytoplankton morphology models will be

260 estimated:

261 - Spheres

262 - Spheres with Spherical Inclusions

263 - Hexahedra with randomly tilted facets

264 - Hexahedra with randomly tilted facets and hexahedral inclusions

265 Consequently, the single-scattering properties of these particles must be computed as an input to the Monte Carlo radiative

266 transfer calculations. Other possible phytoplankton shape models of particular interest to the oceanographic community are

267 of the spheroidal type [49], but have not been considered here. As in the precursor study from [10], the computation of the

268 bulk scattering properties of all particle morphologies is based on a Junge-type distribution with exponent -4. This size

269 distribution is commonly applied to phytoplankton [11,22,50]. The use of Junge type particle size distributions for

270 phytoplankton has been criticized by Risovic, who argues in favor of a segmented Gamma type distribution [51], however a

271 sensitivity study with respect to the size distribution is beyond the scope of this project and corresponding study is already

272 available in [52]. An illustration of particle size distributions for phytoplankton is given in Fig. 11.
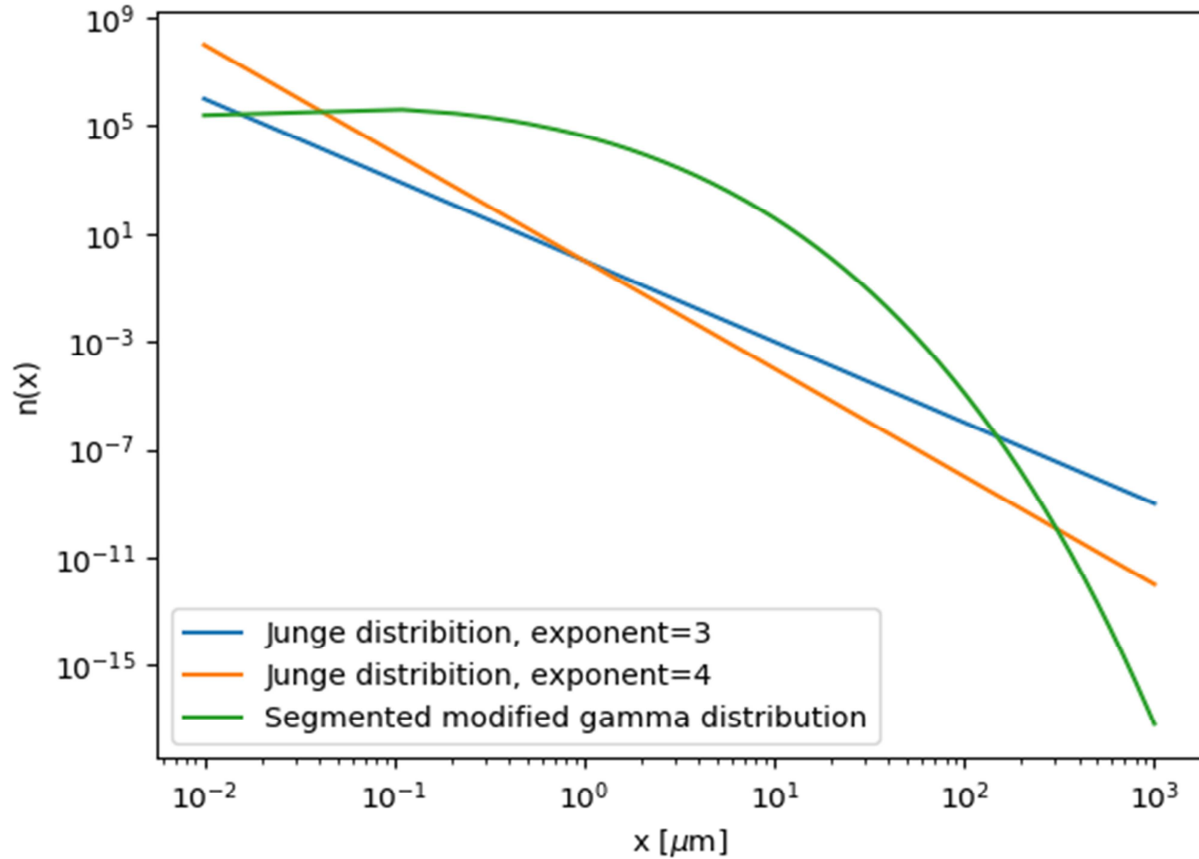
273

275 Figure 11: Typical particle size distributions for phytoplankton in radiative transfer applications. Junge distributions with exponent 3 and 4, and the
276 segmented modified gamma distribution are shown.

277 The complex effective refractive index relative to the surrounding medium of all particle morphologies for this study at the

278 lidar wavelength $\lambda = 532 \; nm$ is selected as $m = 1.05 + i \cdot 0.002$ from [53]. Only one lidar wavelength is considered in

279 the present study, excluding color ratio measurements from scrutiny.

280 For a long time, **spherical particles**, such as the rendering on the right of Fig. 12, have been considered as a first-order

281 approximation in light scattering problems, and this is also the case for phytoplankton (see Ref. [54]). This is due to the

282 early availability of the analytic Lorenz-Mie solution to the scattering problem from Ref. [55] and corresponding efficient

283   solver algorithms for its computation, such as BHMIE from Ref. [56]. Consequently, this type of particle has been included

284   as a baseline reference for the single-scattering properties in this work. Scalar properties, such as the extinction efficiency,

285   are summarized in Table 2 at the end of the section, together with the single-scattering properties of the other morphologies.

286   The scattering phase matrix elements are shown in Fig. 13 in comparison to the elements of a spherical particle with a

287   spherical inclusion discussed below. The bulk scattering properties have been computed based on a size range from 0.001 to

288   10 micrometers with 50 logarithmically spaced abscissae.

289

290   **Spherical particles with spherical inclusions** allow additional freedom in the sense that they allow the modelling of

291   organelles inside the phytoplankton, such as chloroplasts. Phytoplankton chlorophyll molecules (light-harvesting pigment-

292   protein complex) are located in the chloroplasts. These structures absorb the incoming radiation and thus alter the cells'

293   single-scattering properties of cells. This is illustrated in Fig. 12. To ensure comparability with the Mie case, both

294   homogeneous and heterogeneous plankton morphologies should have the same effective refractive index. Specifically, the

295   Bruggeman effective medium approach [57] is selected, that is, effective refractive index m and component indices m_i

296   need to fulfil the following relation for a two-component mixture:

$$\sum_{i=1,2} f_i \cdot \frac{m_i - m}{m_i + 2 \cdot m} = 0, \qquad\qquad (10)$$

298   where f_i is the volume fraction for the i-th component substance. Eq. (10) can be solved analytically. For a volume

299   fraction of 80 % bulk to 20% chloroplast, the refractive indices are:

300   - Bulk: $m_{bulk} = 1.02 + i \cdot 0.0009$

301   - Chloroplast: $m_{inclusion} = 1.175992 + i \cdot 0.006839$

302   This specific volume ratio was chosen mainly due to the computational limitations of the light scattering codes used in this

303   study. To illustrate the difference between a particle with a single effective index of refraction and a particle with an explicit

304   inclusion, a rendering of the two cases is shown in Fig. 12. The coloration of the images is for illustration purposes only,

305   and does not correspond to the real absorption spectrum of phytoplankton. Again, the bulk scattering properties have been

306   computed based on a size range from 0.001 to 10 micrometers with 50 logarithmically spaced abscissae.
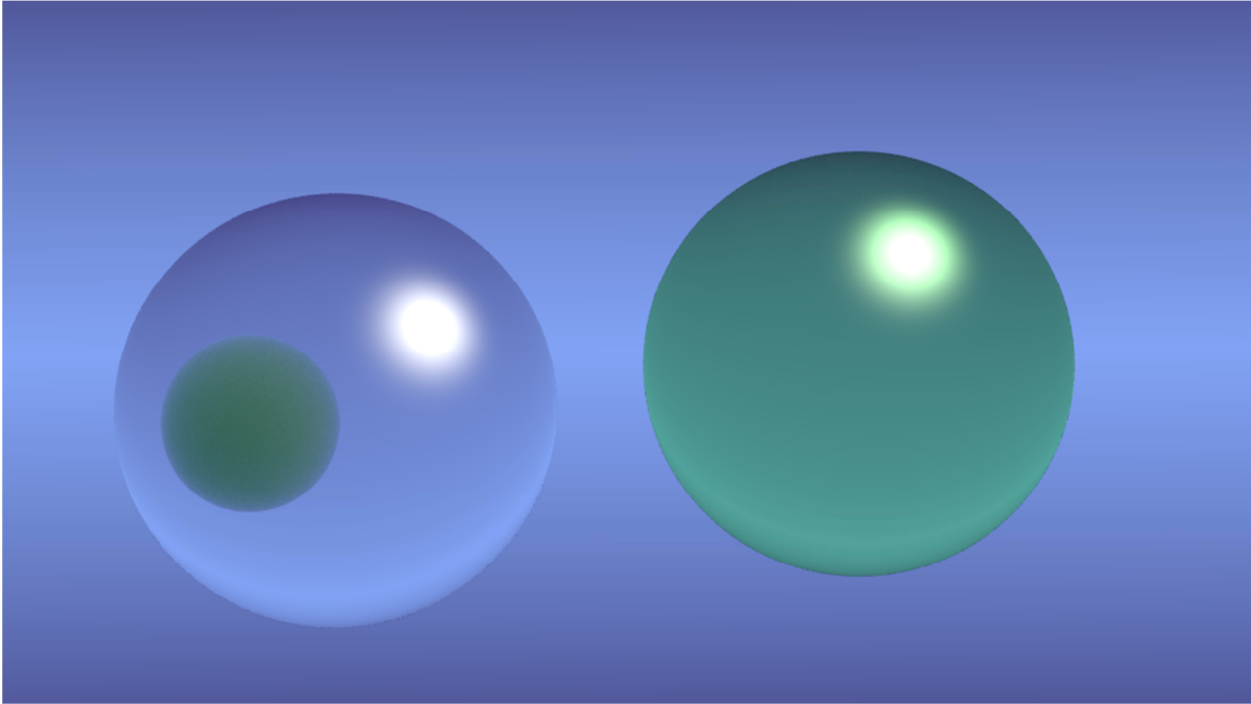
307

Figure 12: Rendering of two spherical particles as phytoplankton models. Left: sphere with spherical inclusion; Right: no inclusion. Both spheres have the same effective refractive index according to Bruggeman mixing. The volume ratio of bulk to inclusion is 80/20. Colour has been added for illustration purposes only and does not correspond to the actual absorption spectrum of phytoplankton.

The single-scattering properties of the spherical particle with spherical inclusion have been computed using the semi-analytic Multiple-Sphere T-Matrix Method by Mackowski and Mishchenko [58]. The phase matrix is shown in Fig. 13 in comparison to the homogeneous case and the scalar properties are listed in Table 2.
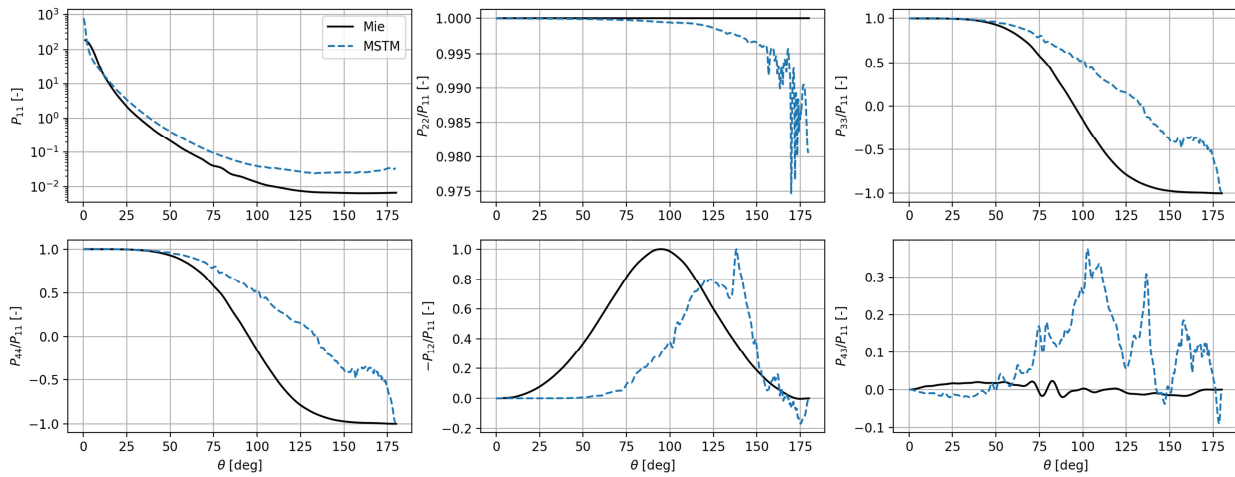

Figure 13: Comparison of bulk phase matrix elements for Mie scattering and the Multiple-Sphere T-Matrix model.

It should be noted that the backscattering part of the Lorenz-Mie phase function in Fig. 13 is similar in magnitude to the values given in 3.10, column 1 of [22]. The MSTM phase function in the backscattering region however is larger by a factor of 3. A similar situation can be observed for the phase functions of the hexahedral particles in Fig. 16, suggesting that this is

320   a consistent effect caused by the presence of an inclusion inside a host particle.

321   **Hexahedra with tilted facets** have been shown in [11] to be a suitable morphology for representing the single-scattering

322   properties of phytoplankton. An ensemble of hexahedra with randomly tilted facets provides an approximation to the

323   stochastic variation of phytoplankton shapes encountered in real lidar measurements. In the same way as in [11], the single-

324   scattering properties of an ensemble similar to the one shown in Fig. 14 have been computed at 532 nm through a

325   combination of the Invariant Imbedding T-Matrix Method (II-TM) from [59,60] and the Physical-Geometric Optics Hybrid

326   Method (PGOH) from [61]. This combination allows to extend the range of computable sizes to 100 µm. The resulting

327   phase matrix is shown in Fig. 16, again in comparison to the case with a single inclusion, and the scalar properties are given

328   in Table 2. An important issue to consider when computing the single-scattering properties of the hexahedral particles is that

329   Eq. (1) requires the assumption that the scattering particles are not only randomly oriented, but also have a plane of

330   symmetry or consist of an equal mixture of particle and mirror-particle. A rigorous analysis of this topic can be found in

331   [62]. To fulfil these requirements, all hexahedra ensembles are defined using an equal number of particles and mirror-

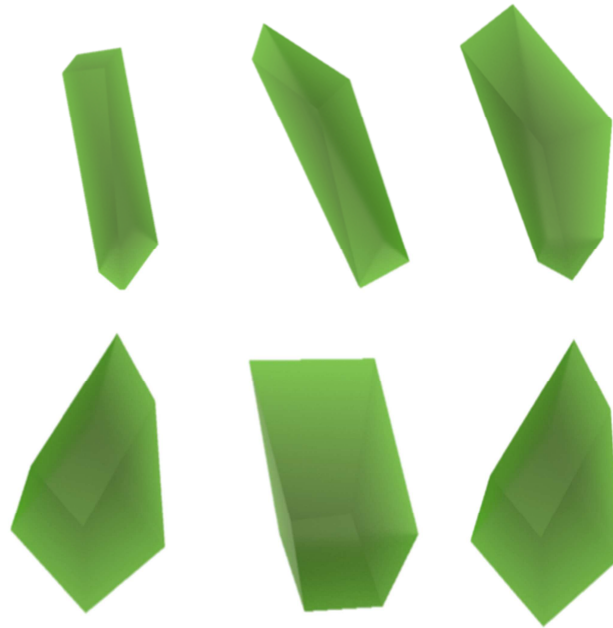332   particles in the present analysis.

333

334   Figure 14: Rendering of ensemble of hexahedra with tilted facets as model particles for the single-scattering properties of phytoplankton. Colour has been
335   added for illustration purposes only.

336   It is obvious from Fig. 16 that the main difference with respect to the spherical model lies in the polarization elements of the

337   phase matrix and the phase function alone is very similar in shape, as is also the case for the sphere with a spherical

338   inclusion.

339

340   **Hexahedra with tilted facets and hexahedral inclusions** represent a matryoshka doll version of the homogeneous

341   hexahedron, as illustrated in Fig. 15. In the present case, the hexahedra with tilted facets contain a smaller hexahedron with

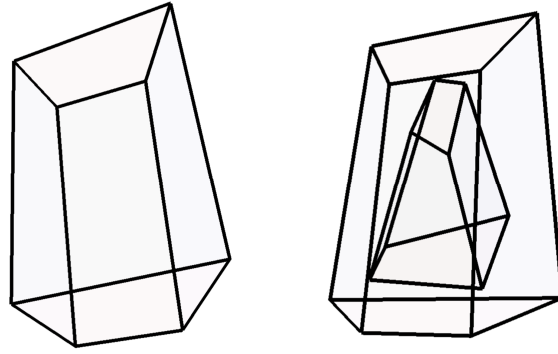342   tilted facets as an inclusion.

343

344 Figure 15: Hexahedron with (right) and without (left) hexahedral inclusion.

345 The single-scattering properties of the hexahedron with inclusions are computed in the same way as for the homogeneous

346 hexahedra ensemble and the parameters, such as the volume fraction, are identical to the spherical inclusion case, such that

347 both homogeneous and inhomogeneous hexahedra share the same effective index of refraction. The resulting phase matrix

348 is shown in Fig. 16 in comparison with the homogeneous case and the scalar single-scattering properties are listed in Table
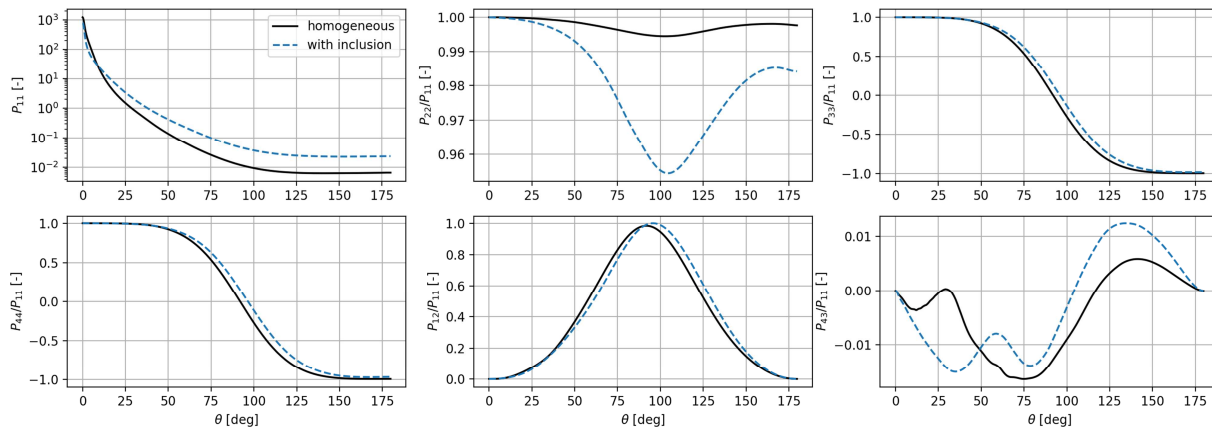
349 2.

350

351 Figure 16: Comparison of bulk phase matrix elements for an ensemble of hexahedra with tiled facets and hexahedra with tilted facets and a single
352 hexahedral inclusion with a volume ration of 80/20.

353 As can be seen from the comparison in Fig. 16, the difference of the phase matrix elements is much less pronounced than

354 for the spherical cases in Fig. 13. The only noticeably different element of the phase matrix is P_{43}. Consequently, it is more

355 difficult to distinguish the homogeneous hexahedron from the hexahedron with inclusion by optical means than in the cases

356 of spheres with or without inclusions.

357 Table 1: Scalar bulk scattering properties of phytoplankton morphology set relevant to the Monte Carlo radiative transfer calculations.

Morphology	Spherical	Spherical w/ inclusion	Hexahedral w/ tilted facets	Hexahedral with inclusion
Extinction efficiency Q_{ext}	2.2581463	1.7048497	0.5154075	0.52472971

Single-scattering albedo $\varpi_{RayleighOcean}$	0.86475996	0.8720722	0.87761955	0.86081396

358

359   The single-scattering albedo of all morphologies is roughly equal (Table 2). As discussed in [11], the extinction efficiency

360   of the hexahedra is much lower than that of the spherical models.

4. Monte Carlo radiative transfer results

361

362   This section discusses the results obtained from the Monte Carlo sensitivity study under variation of different assumptions

363   of the lidar measurement process. Sections 4.1 and 4.2 first validate the convergent solutions by of the Monte Carlo solver.

4.1. Monte Carlo convergence

364

365   To ensure the convergence of the coupled Monte Carlo RT solver, a convergence check has been performed for the case of

366   a homogeneous plankton layer of 20 m thickness using the hexahedral morphology without inclusions. The results of the

367   convergence study are shown in Fig. 17. The total attenuated backscatter (TAB) of the plankton layer has been chosen as a

368   scalar convergence indicator for the expected measurement value, as the integrated AB of the atmosphere above the ocean

369   converges much more quickly. The off-nadir angle of the calculation is 1 degree, the laser divergence angle 10^{-4} degrees,

370   the lidar height 705 km and the source Stokes vector linearly polarized, as in Eq. (2).
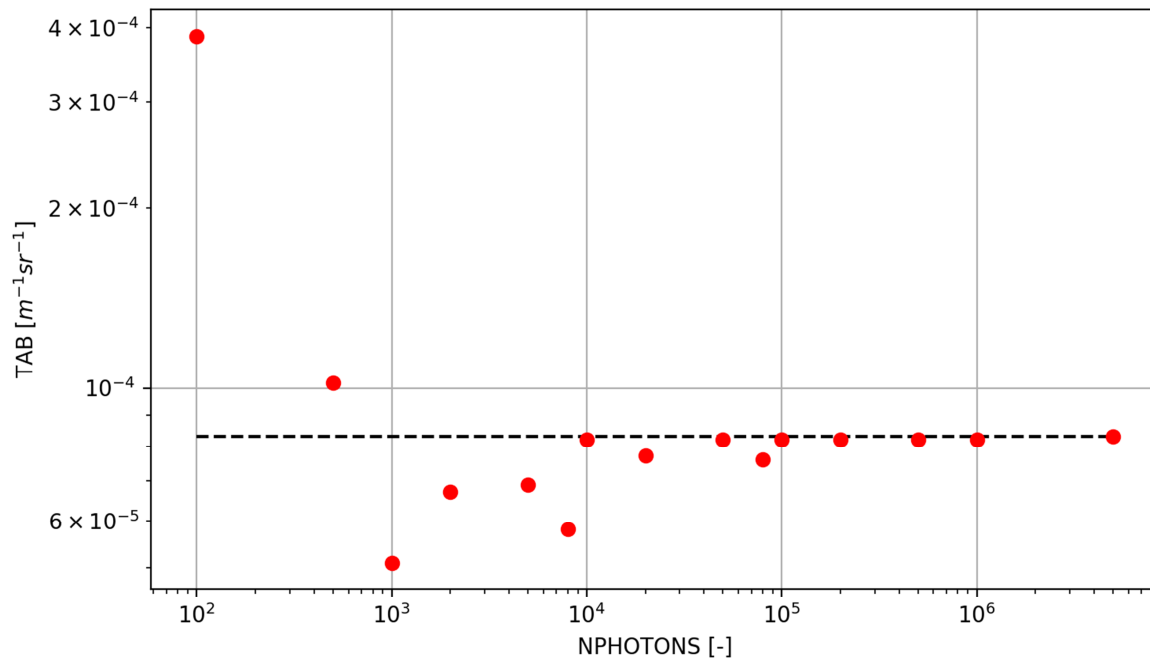

371

372   Figure 17: Convergence of the total attenuated backscatter of the homogeneous test plankton layer as a function of Monte Carlo photons.

373   Fig. 17 indicates that convergence is achieved after 10^5 Monte Carlo trajectories, but all further calculations in this section

374   are carried out using $4 \cdot 10^6$ Monte Carlo trajectories. This is facilitated by the efficiency of the variance reduction

375   technique.

376   *4.2. Monte Carlo validation*

377   After a condition for the convergence of the Monte Carlo code has been determined, the validity of the scattering results of

378   the code is checked against analytical results. For the validation, in Fig. 18 the Monte Carlo code was compared against an

379   analytical relationship given by Eq. (4) of [63], and the solution of the lidar equation in the single scattering case in Fig. 19.

380   The comparison was carried out for a single cloud layer with an effective radius of 10 µm. As can be seen, the Monte Carlo

381   results follow the analytic relationships to an acceptable degree.

382
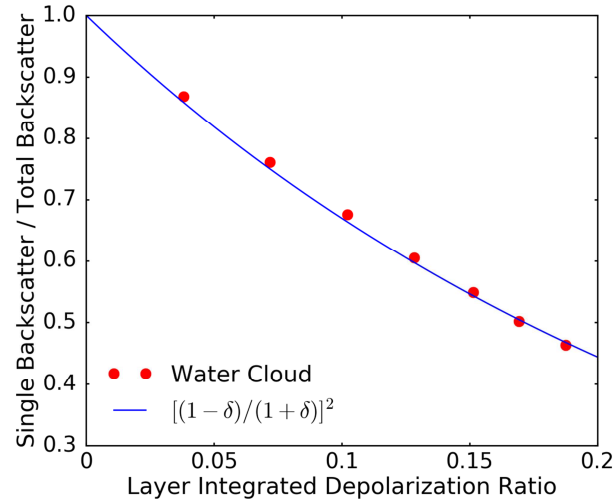

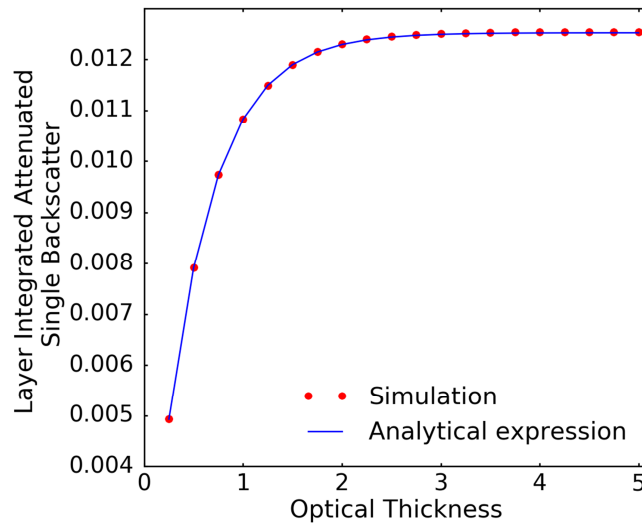383   Figure 18: Comparison between simulated and analytical η-δ relations

384

385   Figure 19: Comparison between simulated Monte-Carlo and analytical layer integrated attenuated single backscatter at various optical thickness.

386   *4.3. Sensitivity to lidar off-nadir angle*

387   In the practical analysis of lidar signals from oceans, off-nadir data may be selected to avoid the specular reflection from the

388   ocean surface, or to obtain multi-angle observations. For this reason, Monte Carlo calculations for a single, 10 m

389   phytoplankton layer of hexahedral particles have been performed, investigating zero, 0.5, and 1 degree off-nadir angle.

390   While there are no substantial differences in the attenuated backscatter for these small angles, there is a noticeable reduction

391   in the depolarization ratio (Fig. 20).
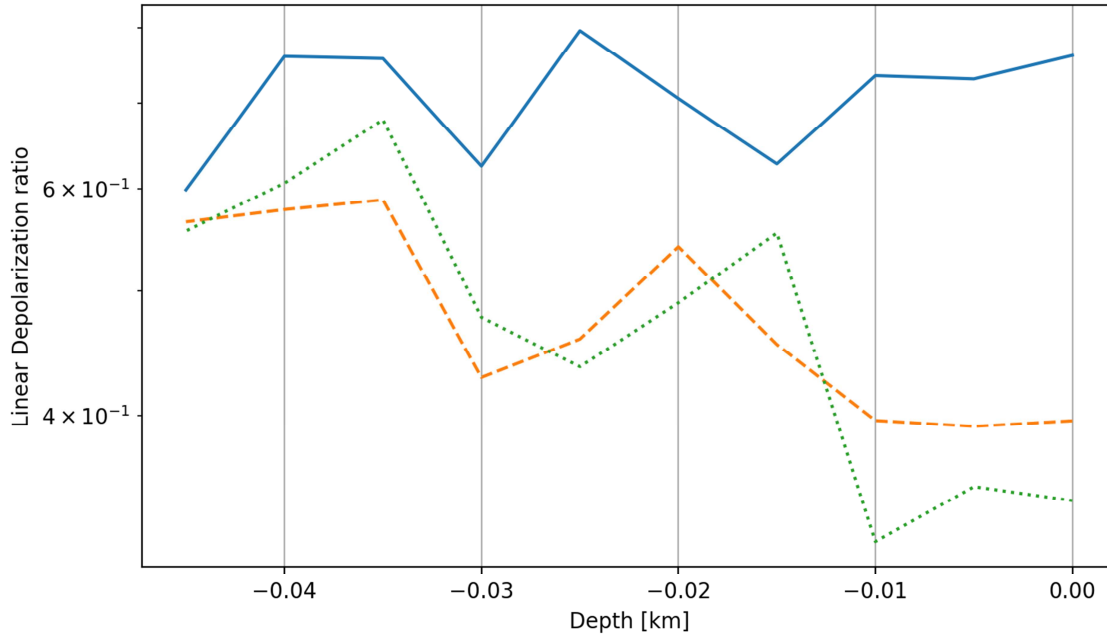

392

393   Figure 20: Linear depolarization ratio over ocean depth. Off-nadir angles are shown in blue (0 degrees), orange (0.5 degrees), and green (1 degree).

394   *4.4. Sensitivity to ocean surface roughness*

395   The preceding test case was likewise used to study the effect of increasing ocean surface roughness. Using the Cox-Munk

396   spectrum, wind speeds of $U_{wind} = 5$ and $10\,m \cdot s^{-1}$ have been investigated for a zero degree off-nadir angle. Following

397   [23], the standard deviation σ_{θ_n} of the Gaussian probability distribution from which the azimuth angle θ_n of the ocean

398   surface normal vector is sampled is given by the following expression:

399    $$\sigma_{\theta_n} = \left(0.003 + 0.00512 \cdot U_{wind} \right). \tag{11}$$

400   This leads to a standard deviation of 0.0286 and 0.0542 for 5 and 10 m s^{-1} windspeed, respectively. There is only a slight

401   decrease of the attenuated backscatter near the ocean surface with increased wind speed, but no appreciable difference in the

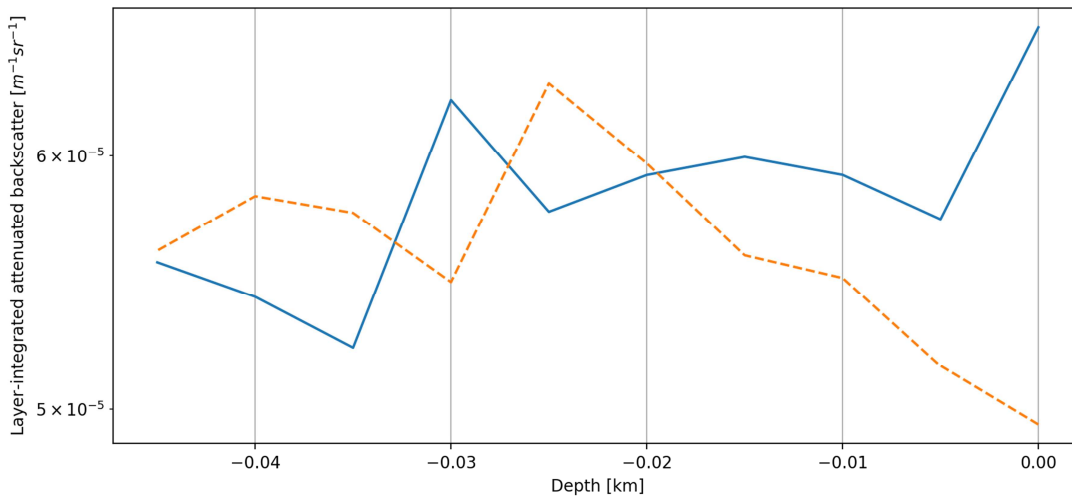402   depolarization ratio (Fig. 21).

403

Figure 21: Attenuated backscatter for 5 (blue) and 10 (orange) m s^{-1} windspeeds at the ocean surface.

404

405   *4.5. Sensitivity to phytoplankton morphology*

406   The sensitivity study of lidar attenuated backscatter and linear depolarization ratio is carried out with all four morphology

407   types discussed above. The same test geometry as in the previous cases has been kept. There is a slight dependence of the

408   attenuated backscatter (Fig. 22) on the phytoplankton morphology, and a somewhat stronger dependence for the

409   depolarization ratio shown in Fig. 23. However, the difference between spherical and non-spherical particle is more

410   pronounced than to the respective cases with inclusions, which adequately justifies the effective medium approach.
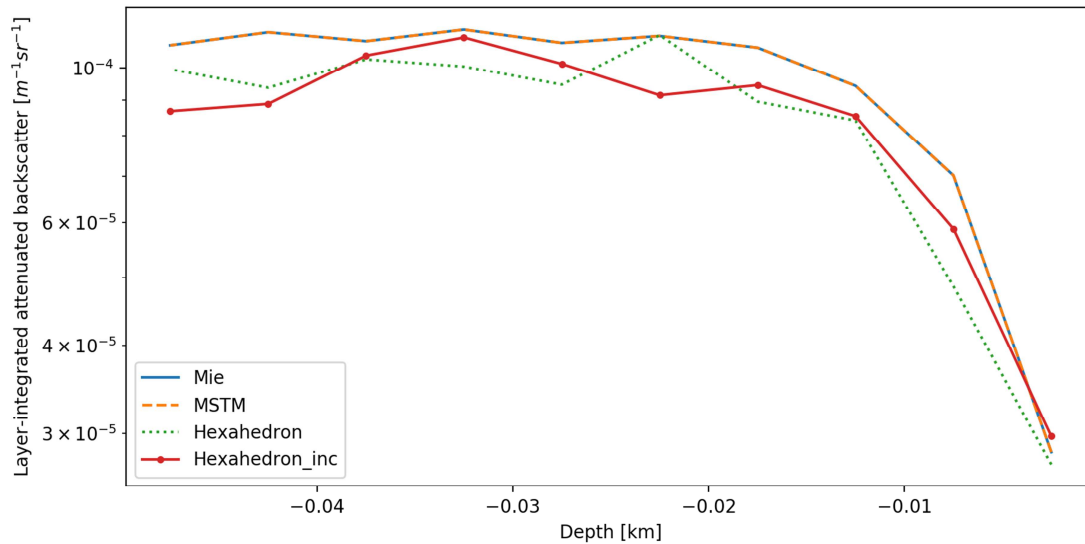

411

412   Figure 22: Attenuated backscatter vs. ocean depth for four different phytoplankton morphologies. Note that spherical particles have a slightly higher AB
413   than nonspherical particles.
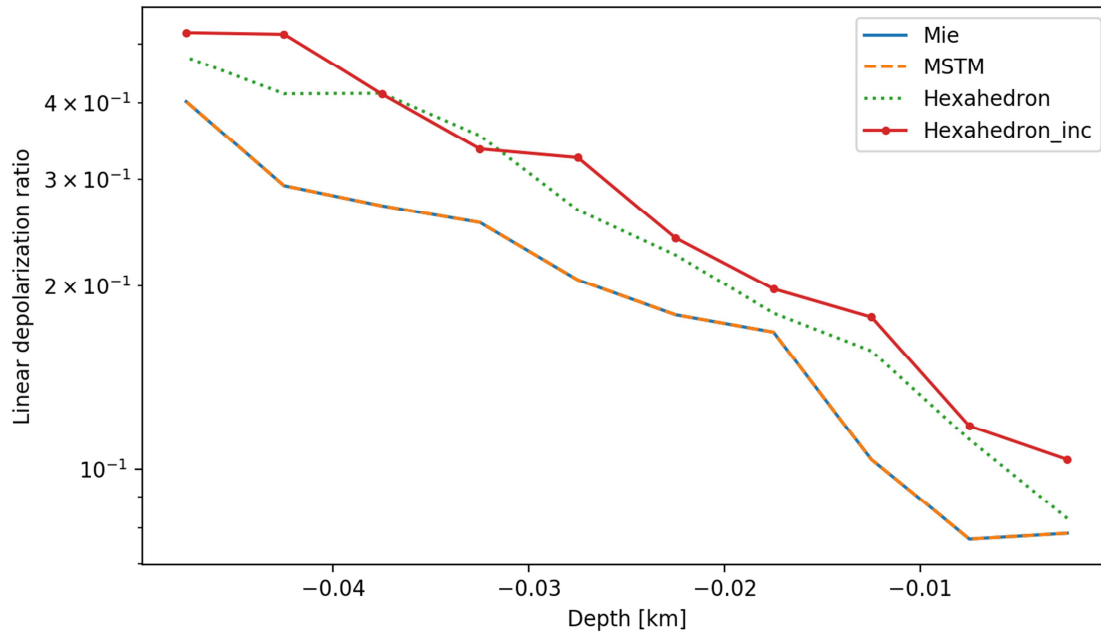
Figure 23: Linear depolarization ratio vs ocean depth for four different phytoplankton morphologies. Note the consistent offset between spherical and non-spherical particles.

4.6. Sensitivity to phytoplankton vertical profile

Lastly, the influence of an inhomogeneous vertical profile of the plankton is investigated. For this case, the profile in Fig. 10 has been selected and discretized into layers, each of which is 30 m thick. The hexahedra with tilted facets have been selected as a scattering morphology and all results have been computed with $6 \cdot 10^6$ initial Monte Carlo trajectories. As can be seen from the layer-integrated attenuated backscatter results as a function of the ocean depth shown in Fig. 24, a strong influence of the phytoplankton density profile is indicated. No such dependence is found for the depolarization ratio. For comparison, the normalized phytoplankton carbon biomass density taken from Fig. 10, which serves as a proxy for the total phytoplankton density in the present case is also shown in Fig. 24. However, the attenuated backscatter result is also negatively impacted by layer discretization artifacts and the rapidly declining optical depth of the individual layers makes it difficult to achieve convergence in the Monte Carlo calculations. A reduced peak of the attenuated backscatter or undershoot at each layer interface is clearly visible in Fig. 24. To investigate the discretization issue further, another attenuated backscatter result with a layer resolution that is twice as high (i.e. 15 m layer depth) is also shown in Fig. 24. As such, future investigations of radiative transfer involving phytoplankton density profiles should require a smooth variation of the optical properties. It is also clear that for the current model setup increasing the spatial resolution of the layers leads to a lower total optical depth in regions where the phytoplankton carbon biomass density is below its maximum (i.e. in light or nutrient limited growth regions). This also reduces the attenuated backscatter signal, as can be seen clearly in Fig. 24 in the difference between the 30 m and 15 m layer discretization in the light limited region. There is a clear correspondence to the sharply decreasing extinction coefficient of the phytoplankton layers shown in Fig. 10. Consequently, these results

435   provide an indication that lidar measurements are quite sensitive towards a variation of phytoplankton concentration in the

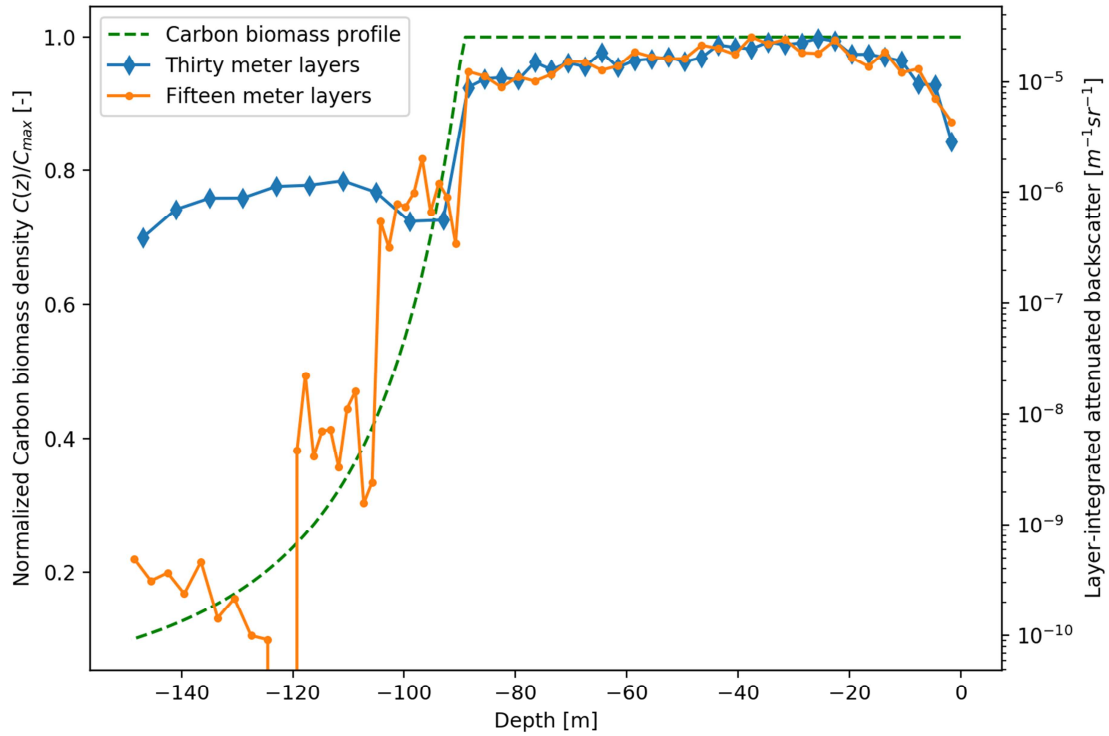436   vertical direction.

437

438   Figure 24: Layer-integrated attenuated Backscatter for the inhomogeneous phytoplankton profile shown in Fig. 7.

439   A comparison of the results for an inhomogeneous case in Fig. 24 to the results for a homogeneous case in Fig. 25 reveals

440   that the mixed layer depth can be clearly identified from the phytoplankton attenuated backscatter signal under the current

441   model assumptions and that the decline of the phytoplankton carbon biomass density below the mixed layer depth leads to a

442   significantly lower attenuated backscatter signal that strongly correlates with the spatial distribution of the carbon density.

443   The discontinuity in the TAB signal in the transition zone from the mixed layer to the light limited region must again be

444   considered an artefact of the Monte Carlo layer discretization and in reality a discontinuity in the first derivative of the TAB

445   signal (i.e. a kink), and not the TAB signal itself, is to be expected.
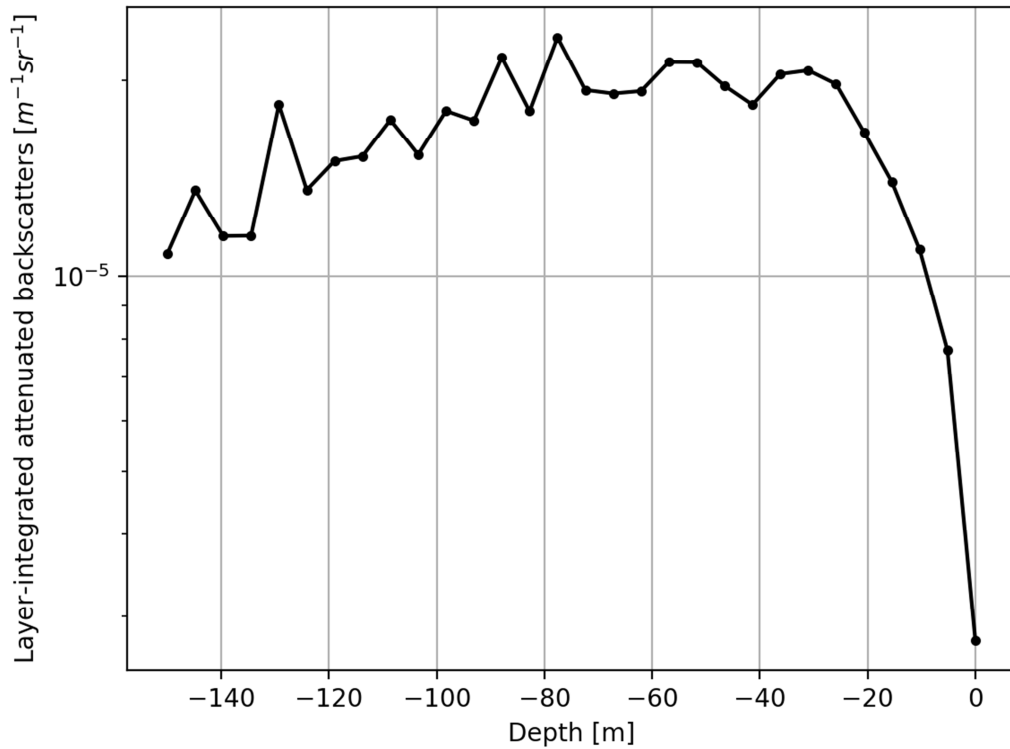
446

Figure 25: Layer-integrated attenuated Backscatter for a homogeneous phytoplankton profile in contrast to Fig. 22.

5. Conclusion

In this study, a 3D polarized Monte Carlo RTE solver for lidar applications involving a coupled atmosphere-ocean system was developed in conjunction with a semi-implicit solver for the time-dependent population balance equation of buoyant phytoplankton. Furthermore, the single-scattering properties of different phytoplankton model morphologies were computed. This allows an in-depth sensitivity study of spaceborne lidar attenuated backscatter and depolarization ratio measurements that facilitate studies of the global accounting and taxonomy of phytoplankton biomass and NPP in the oceans. The present sensitivity study indicates that both particle morphology and phytoplankton vertical density variation have strong impacts on lidar measurement. Lidar polarization is identified as a useful parameter for investigating phytoplankton morphology, however, it is not expected to be strongly influenced by morphological details, such as inclusions, which is in contrast to the measured phase matrices of Volten et al. (1998) [64]. Possible explanations for this discrepancy are: 1.) Volten specifically addresses gas vacuoles, and not chlorophyll; 2.) the idealized conditions of the numerical experiment conducted in this manuscript; 3.) the exact matching of the effective refractive index of the particle with and without inclusion in the numerical experiments, which is not possible for measurements in nature. The better investigate the significant effect of phytoplankton vertical profiles, it is necessary to improve discretized RT simulations. In particular Invariant-Imbedding RT solvers [65,66] are considered more efficient when it comes to smooth vertical variations in the underlying atmospheric and oceanic profiles.

Acknowledgements

This study was supported by the National Science Foundation (NSF) (AGS-1338440, OCE-1459180) and partially supported by the endowment funds associated with the David Bullock Harris Chair (02-51223110000) in Geosciences at the Texas A&M University. A substantial amount of the calculations for this study were carried out at the Texas A&M University Supercomputing Facilities, and the help and assistance of the facility staff is gratefully acknowledged. The authors would like to thank Dr. George Kattawar for sharing his considerable experience in Monte Carlo radiative transfer calculations of oceans.

Appendix A.

The depth-resolved phytoplankton NPP code is available as a github repository at https://github.com/PStegmann/Westberry_08_model and is licensed under the GPL v3.0.

References

[1] Field, C. B., M. J. Behrenfeld, J. T. Randerson, and P. Falkowski (1998): Primary Production of the Biosphere: Integrating Terrestrial and Oceanic Components. Science 281, 237-40.

[2] Morel, A., and D. Antoine (2002): Small Critters – Big Effects. Science 296, 1980-1982.

[3] Gordon, H. R., and W. R. McCluney (1975): Estimation of the Depth of Sunlight Penetration in the Sea for Remote Sensing. Appl. Opt. 14, 413-6.

[4] Uitz, J., H. Claustre, A. Morel, and S. B. Hooker (2006): Vertical distribution of phytoplankton communities in open ocean: An assessment based on surface chlorophyll. J. Geophys. Res.: Oceans 111, C08005.

[5] Winker, D. M. et al. (2009): Overview of the CALIPSO Mission and CALIOP data processing algorithms. J. Atmos. Ocean Technol. 26, 2310-2323.

[6] Churnside, J. H., B. J. McCarty, and X. Lu (2013): Subsurface ocean signals from an orbiting polarization lidar. Remote Sens. 5, 3457-3475.

[7] Behrenfeld, M. J., (2013): Space-based lidar measurements of global carbon stocks.

[8] Behrenfeld, M. J., Y. Hu, R. T. O'Malley, E. S. Boss, C. A. Hostetler, D. A. Siegel, J. L. Sarmiento, J. Schulien, J. W. Hair, X. Lu, S. Rodier, and A. J. Scarino (2016): Annual boom-bust cycles of polar phytoplankton biomass revealed by space-based lidar. Nature Geoscience

[9] Schulien, J. A., M. J. Behrenfeld, J. W. Hair, C. A. Hostetler, and M. S. Twardowski (2017): Vertically- resolved phytoplankton carbon and net primary production from a high spectral resolution lidar. Optics Express 25(12), 13577-87

[10] Hu, Y.-X., D. Winker, P. Yang, B. Baum, L. Poole, and L. Vann (2001): Identification of cloud phase from PICASSO-CENA lidar depolarization: a multiple scattering sensitivity study. J. Quant. Spec. Rad. Trans. 70

[11] Xu, G., B. Sun, S. D. Brooks, P. Yang, G. W. Kattawar, X. Zhang (2017): Modeling the inherent optical properties of aquatic particles using an irregular hexahedral ensemble. J. Quant. Spec. Rad. Trans. 191, 30-39.

[12] Chandrasekhar, S. (1960): *Radiative Transfer*. Mineola, NY: Dover Publications.

[13] Mishchenko, M. I., J. M. Dlugach, M. A. Yurkin, L. Bi, B. Cairns, L. Liu, R. L. Panetta, L. D. Travis, P. Yang, and N. T. Zakharova (2016): First-principles modeling of electromagnetic scattering by discrete and discretely heterogeneous random media. Physics Reports 632, 1-75.

[14] Pierrat, R., P. Ambichl, S. Gigan, A. Haber, R. Carminati, and S. Rotter (2014): Invariance property of wave scattering through disordered media. PNAS 111(50), 17765-70.

[15] Mishchenko, M. I. (2008): Multiple scattering by particles embedded in an absorbing host medium. 2. Radiative transfer equation. J. Quant. Spec. Rad. Trans. 109, 2386-2390.

[16] Mishchenko, M. I., and P. Yang (2018): Far-field Lorenz-Mie scattering in an absorbing host medium: theoretical formalism and FORTRAN program. J. Quant. Spec. Rad. Trans. 205, 241-52.

[17] Spanier, J., and E. M. Gelbard (1969): *Monte Carlo Principles and Neutron Transport Problems*. Mineola, NY: Dover Publications.

[18] Poole, L. R., D. D. Venable, and J. W. Campbell (1981): Semianalytic Monte Carlo radiative transfer model for oceanographic lidar systems. Applied Optics 20(20), 3653-56

504   [19] Iwabuchi, H. (2006): Efficient Monte Carlo Methods for Radiative Transfer Modeling. J. Atmos. Sci. 63, 2324-39.

505   [20] Buras, R., and B. Mayer (2011): Efficient unbiased variance reduction techniques for Monte Carlo simulations of radiative transfer in cloudy
506   atmospheres: The solution. J. Quant. Spec. Rad. Trans. 112, 434-47.

507   [21] Whitted, T. (1980): An Improved Illumination Model for Shaded Display. Communications of the ACM 23, 343-9.

508   [22] Mobley, C. D. (1994): *Light and Water: Radiative Transfer in Natural Waters*. Academic Press, San Diego.

509   [23] Cox, C., and W. Munk (1954): Measurement of Roughness of the Sea Surface from Photographs of the Sun's Glitter. J. Opt. Soc. Am. 44, 838-50.

510   [24] Stegmann, P. G., C. Tropea, E. Järvinen, M. Schnaiter (2016): Comparison of measured and computed phase functions of individual tropospheric ice
511   crystals. J. Quant. Spec. Rad. Trans. 178, 379-89.

512   [25] Mobley, C. D. (2015): Polarized reflectance and transmittance properties of windblown sea surfaces. Appl. Opt. 54, 4828-49.

513   [26] Ge, L., K. F. Cheung, and M. H. Kobayashi (2008): Stochastic Solution for Uncertainty Propagation in Nonlinear Shallow-Water Equations. J. Hyd.
514   Eng. 134(12), 1732-43.

515   [27] Zhai, P.-W., G. W. Kattawar, and Y. Hu (2012): Comment on the transmission matrix for a dielectric interface. J. Quant. Spec. Rad. Tran. 113, 1981-
516   1984.

517   [28] Kattawar, G. W., and C. N. Adams (1989): Stokes vector calculations of the submarine light field in an atmosphere-ocean with scattering according
518   to a Rayleigh phase matrix: Effect of interface refractive index on radiance and polarization. Limnol. Oceanogr. 34(8), 1453-1472.

519   [29] Elterman, L. (1964): Atmospheric Attenuation Model, 1964, in the Ultraviolet, Visible, and Infrared Regions for Altitudes to 50km. Env. Res. Pap.
520   46, Air Force Cambridge Research Laboratories, Hanscom Fields, Mass.

521   [30] U.S. Standard Atmosphere, 1962, U.S. Government Printing Office, Washington D.C. (1962).

522   [31] Wendisch, M., and P. Yang (2011): *Theory of Atmospheric Radiative Transfer*. Wiley-VCH Weinheim, Germany.

523   [32] Pham Thi, N. N., J. Huisman, and B. P. Sommeijer (2005): Simulation of three-dimensional phytoplankton dynamics: competition in light-limited
524   environments. J. Comp. Appl. Math. 174, 57-77.

525   [33] Hundsdorfer, W., J. G. Verwer (2003): Numerical Solution of Time-Dependent Advection-Diffusion-Reaction Equations. Springer Series in
526   Computational Mathematics 33, Springer Berlin-Heidelberg.

527   [34] Godunov, S. K. (1959): A difference scheme for numerical computation of discontinuous solution of hyperbolic equation. Math. Sbornik 47, 271-306.

528   [35] Monod, J. (1949): The Growth of Bacterial Cultures. Annual Review of Microbiology 3, 371. doi:10.1146/annurev.mi.03.100149.002103

529   [36] Westberry, T. K., and M. J. Behrenfeld (2014): Oceanic Net Primary Production. *Biophysical Applications of Satellite Remote Sensing*, Chapter 8,
530   Springer Heidelberg New York.

531   [37] Westberry, T., M. J. Behrenfeld, D. A. Siegel, and E. Boss (2008): Carbon-based primary productivity modeling with vertically resolved
532   photoacclimation. Global Biogeochm. Cycl. 22, GB2024, doi:10.1029/2007GB003078 .

533   [38] Anderson, T. R. (1993): A spectrally averaged model of light penetration and photosynthesis. Limnol. Oceanogr. 38(7), 1403-19.

534   [39] Wick, G. C. (1954): Properties of the Bethe-Salpeter Wave Functions. Phys. Rev. 96(4), 1124-34.

535   [40] Feynman, R. P., A. R. Hibbs, and D. F. Styer (2010): *Quantum Mechanics and Path Integrals*. Mineola NY: Dover Publications.

536   [41] Petty, G. W. (2006): A First Course in Atmospheric Radiation. Madison, WI: Sundog Publishing.

537   [42] Morel, A., and S. Maritorena (2001): Bio-optical properties of oceanic waters: A reappraisal. J. Geophys. Res. 106(C4), 7163-7180.

538   [43] Stegmann, P. G., and P. Yang (2017): A regional, size-dependent, and causal effective medium model for Asian and Saharan mineral dust refractive
539   index spectra. J. Aer. Sci. 114, 327-41.

540   [44] Kruk, C., V. L. M. Huszar, E. T. H. M. Peeters, S. Bonilla, L. Costa, M. Lürling, C. S. Reynolds, and M. Scheffer (2010): A morphological
541   classification capturing functional variation in phytoplankton. Freshwater Biology 55, 614-27.

542   [45] van de Hulst, H. C. (1981): *Light Scattering by Small Particles*. Mineola, NY: Dover Publications.

543   [46] Sun, B., G. W. Kattawar, P. Yang, M. S. Twardowski, and K. M. Sullivan (2016): Simulation of the scattering properties of a chain-forming
544   triangular prism oceanic diatom. J. Quant. Spec. Rad. Trans. 178, 390-99.

545   [47] Charon, J., S. Blanco, J.-F. Cornet, J. Dauchet, M. El Hafi, R. Fournier, M. K. Abboud, and S. Weitz (2016) : Monte Carlo implementation of
546   Schiff's approximation for estimating radiative properties of homogeneous, simple-shaped and optically soft particles : Application to photosynthetic
547   micro-organisms. J. Quant. Spec. Rad. Trans. 172, 3-23.

548   [48] Yurkin, M. A., V. P. Maltsev, and A. G. Hoekstra (2007): The discrete dipole approximation for simulation of light scattering by particles much
549   larger than the wavelength. J. Quant. Spec. Rad. Trans. 178, 325-35.

550   [49] Clavano, R. W., E. Boss, and L. Karp-Boss (2007): Inherent optical properties of non-spherical marine-like particles – from theory to observation.
551   Ocean. Mar. Bio.: An Annual Review 45, 1-38.

[50] Kattawar, G. W., G. N. Plass, and J. A. Guinn, Jr. (1973): Monte Carlo Calculations of the Polarization of Radiation in the Earth's Atmosphere-Ocean System. J. Phys. Ocean. 3(4), 353-72.

[51] Risovic, D. (1993): Two component model of the sea particle size distribution. Deep-Sea Res. Part I Oceanogr. Res. Papers 40, 1459-73.

[52] Risovic, D. (2002): Effect of suspended particulate-size distribution on the backscattering ratio in the remote sensing of seawater. Applied Optics 41(33), 7092-7101.

[53] Jonasz, M., and G. Fournier (2007): Light Scattering by Particles in Water: Theoretical and Experimental Foundations. Cambridge MS: Academic Press.

[54] Mobley, C. D., B. Gentili, H. R. Gordon, Z. Jin, G. W. Kattawar, A. Morel, P. Reinersman, K. Stamnes, R. H. Stavn (1993): Comparison of numerical models for computing underwater light fields. Applied Optics 32(36), 7484-504.

[55] Mie, G. (1908): Beiträge zur Optik trüber Medien, speziell kolloidaler Metallösungen. Annalen der Physik 4(25), 377-445.

[56] Bohren, C. F., and D. R. Huffman (1993): *Absorption and Scattering of Light by Small Particles*. New York: Wiley.

[57] Bruggeman, D. A. G. (1935): Berechnung verschiedener physikalischer Konstanten von heterogenen Substanzen, 1. Dielektrizitätskonstanten und Leitfähigkeiten der Mischkörper aus isotropen Substanzen. Annalen der Physik 5(24), 636-664.

[58] Mackowski, D. W. (2014): A general superposition solution for electromagnetic scattering by multiple scattering domains of optically active media. J. Quant. Spec.. Rad. Trans. 205, 241-252.

[59] Bi, L., P. Yang, G. W. Kattawar, and M. I. Mishchenko (2013): Efficient implementation of the invariant imbedding T-matrix method and the separation of variables method applied to large nonspherical inhomogeneous particles. J. Quant. Spec. Rad. Trans. 116, 169-83. doi:10.1016/j.jqsrt.2012.11.014

[60] Bi, L., and P. Yang (2014): Accurate simulation of the optical properties of atmospheric ice crystals with the invariant imbedding T-matrix method. J. Quant. Spec. Rad. Trans. 138, doi:10.1016/j.jqsrt.1014.01.013

[61] Bi, L., G. W. Kattawar, Y. Hu, and B. Baum (2011): Scattering and absorption of light by ice particles: solution by a new physical-geometric optics hybrid method. J. Quant. Spec. Rad. Trans. 112, 1492-1508. doi:10.1016/j.jqsrt.2011.02.015

[62] Mishchenko, M. I., and M. A. Yurkin (2017): On the concept of random orientation in far-field electromagnetic scattering by nonspherical particles. Opt. Lett. 42, 494-497.

[63] Hu, Y. (2010): Depolarization ratio- effective lidar ratio relation: Theoretical basis for space lidar cloud phase discrimination. Geophys. Res. Lett. 34, L11812.

[64] Volten, H., J. F. de Haan, J. W. Hovenier, R. Schreurs, W. Vassen, A. G. Dekker, H. J. Hoogenboom, F. Charlton, and R. Wouts (1998): Laboratory measurements of angular distributions of light scattered by phytoplankton and silt. Limnol. Oceanogr. 43(6), 1180-97.

[65] Sato, M., K. Kawabata, and J. E. Hansen (1977): A Fast Invariant Imbedding Method for Multiple Scattering Calculations and an Application to Equivalent Widths of CO_2 Lines on Venus. The Astrophys. J. 216, 947-62.

[66] Mishchenko M. I. (1989): The Fast Invariant Imbedding Method for Polarized Light: Computational Aspects and Numerical Results for Rayleigh Scattering. J. Quant. Spec. and Rad. Trans. 43(2), 163-71.